

## RESEARCH ARTICLE

10.1029/2017JD028224

## Key Points:

- Polar mesospheric cloud frequencies decline rapidly in July 2014 due to a two-day wave-driven warming of the mesopause region
- Wintertime planetary waves lead to anomalous temperatures at low latitudes, enhanced extratropical wind shear, and two-day wave growth
- The response of polar mesospheric clouds to the two-day wave-driven temperature increase is modulated by a large mesospheric five-day wave

## Correspondence to:

J. A. France,  
jeffrey.france@colorado.edu

## Citation:

France, J. A., Randall, C. E., Lieberman, R. S., Harvey, V. L., Eckermann, S. D., Siskind, D. E., et al. (2018). Local and remote planetary wave effects on polar mesospheric clouds in the Northern Hemisphere in 2014. *Journal of Geophysical Research: Atmospheres*, 123, 5149–5162. <https://doi.org/10.1029/2017JD028224>








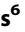
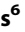
Received 20 DEC 2017

Accepted 26 APR 2018

Accepted article online 5 MAY 2018

Published online 25 MAY 2018

## Local and Remote Planetary Wave Effects on Polar Mesospheric Clouds in the Northern Hemisphere in 2014

J. A. France<sup>1,2</sup> , C. E. Randall<sup>1,3</sup> , R. S. Lieberman<sup>2</sup> , V. L. Harvey<sup>1,3</sup> , S. D. Eckermann<sup>4</sup> , D. E. Siskind<sup>4</sup> , J. D. Lumpe<sup>5</sup> , S. M. Bailey<sup>6</sup> , J. N. Carstens<sup>6</sup> , and J. M. Russell III<sup>7</sup>
<sup>1</sup>Laboratory for Atmospheric and Space Physics, University of Colorado Boulder, Boulder, CO, USA, <sup>2</sup>GATS, Inc., Boulder, CO, USA, <sup>3</sup>Department of Atmospheric and Oceanic Sciences, University of Colorado Boulder, Boulder, CO, USA, <sup>4</sup>Space Science Division, U.S. Naval Research Laboratory, Washington, DC, USA, <sup>5</sup>Computational Physics, Inc., Boulder, CO, USA, <sup>6</sup>Bradley Department of Electrical and Computer Engineering, Virginia Tech, Blacksburg, VA, USA, <sup>7</sup>Center for Atmospheric Sciences, Hampton University, Hampton, VA, USA

**Abstract** Observations by the Cloud Imaging and Particle Size (CIPS) instrument on the Aeronomy of Ice in the Mesosphere (AIM) satellite show an anomalous decline in Northern Hemisphere polar mesospheric clouds (PMCs) from 26 July to 6 August 2014. The decline is attributed to local warming associated with the quasi-two-day wave and interhemispheric coupling (IHC) triggered by planetary wave breaking in the Antarctic (winter) stratosphere. The results indicate that the IHC in 2014 occurred via a pathway that previous studies have not emphasized. Based on observations from the Aura Microwave Limb Sounder (MLS) and reanalyses from both the Modern-Era Retrospective analysis for Research and Applications, Version 2 (MERRA-2) and the Navy Global Environmental Model (NAVGEN), we argue that a strengthening of the summer easterly jet gave rise to enhanced meridional and vertical shear along its equatorward flank, which supported growth of the two-day wave. The two-day wave led to enhanced meridional mixing in northern midlatitudes and a weakening of the northern branch of the mesospheric residual circulation, reducing ascent and warming the polar summer mesopause. In 2014, the five-day planetary wave modulated the response to IHC such that PMCs persisted in its cold phases even though zonal mean temperatures were too high to support PMCs, and were absent in the warm phases when zonal mean temperatures were low enough to support PMCs.

## 1. Introduction

The formation of polar mesospheric clouds (PMCs) depends strongly on the thermal and dynamical conditions that occur near the summer polar mesopause. Although this region is continually sunlit in summer, upwelling associated with the gravity wave (GW)-driven residual circulation forces temperatures away from radiative equilibrium, resulting in the lowest temperatures observed in the atmosphere (e.g., Lübken, 1999). Observations and modeling studies have shown that variability in temperature and vertical wind at the polar summer mesopause is correlated with variability in planetary waves (PWs), winds, and temperatures in the winter stratosphere (e.g., Becker et al., 2004; Becker & Fritts, 2006; Becker & Schmitz, 2003; Körnich & Becker, 2010). Since the formation of PMCs is dependent on summer polar mesopause temperatures and water vapor mixing ratios, which are controlled by the vertical wind, PMC occurrence frequency is highly sensitive to variability in the winter hemisphere (Gumbel & Karlsson, 2011; Karlsson et al., 2007; Karlsson, McLandress, & Shepherd, 2009; Karlsson, Randall, et al., 2009; Siskind et al., 2011).

Conventional interhemispheric coupling (IHC) refers here to a specific teleconnection in which changes in the winter stratosphere lead to anomalies in PMC occurrence frequencies. The proposed dynamical chains of cause and effect that support this IHC involve changes in GW filtering in both hemispheres, as follows (e.g., Karlsson, McLandress, & Shepherd, 2009; Karlsson, Randall, et al., 2009; Körnich & Becker, 2010): Quasi-stationary PW activity increases (or decreases, in which case all of the steps that follow occur in the opposite sense) in the winter stratosphere in the vicinity of the westerly polar night jet, leading to enhanced PW dissipation and/or transience that transfers easterly momentum to the mean flow and weakens the jet. Changes in stratospheric GW filtering result in increases in westerly nonorographic GW forcing of the winter mesosphere above the jet, and a resulting westerly acceleration of the mesospheric zonal-mean zonal wind,

leading to a weakening of the mesospheric residual circulation and net descent and warming in the equatorial mesosphere (e.g., Andrews et al., 1987, see their Figure 6.7b; Becker & Schmitz, 2003; Becker et al., 2004; de Wit et al., 2015; Karlsson & Becker, 2016; Körnich & Becker, 2010). The warm anomaly in the equatorial mesosphere leads to a westerly zonal wind anomaly in the summer hemisphere mesosphere via the thermal wind relation. The westerly wind anomaly in the summer hemisphere causes nonorographic GWs to break at lower altitudes (Körnich & Becker, 2010), which leads to a weakening and lowering of the summer mesospheric residual circulation that ultimately results in warming at the polar summer mesopause via reduced mean ascent, and thus fewer PMCs.

Another source of variability that has been linked to changes in PMC occurrence frequencies is the mesospheric quasi-two-day wave (Lieberman, 1999, 2002; McCormack et al., 2009, 2010; Salby, 1981; Siskind & McCormack, 2014). Siskind and McCormack (2014) found that in January 2005 and 2006, a large two-day wave in the summer midlatitude mesosphere coincided with 8–12 K mean temperature enhancements at the polar summer mesopause. They suggested that deposition of easterly momentum via dissipation of the two-day wave weakened the mesospheric residual circulation, leading to less ascent in the summer polar mesosphere, and thus fewer PMCs.

The mesospheric five-day wave is another source of PMC variability (e.g., Merkel et al., 2003; Nielsen et al., 2010; von Savigny et al., 2007), which affects PMCs via temperature oscillations in the PMC region, leading to enhanced PMC occurrence in the cold phase and fewer PMCs in the warm phase. Using observations from the Student Nitric Oxide Explorer (SNOE) satellite between 1998 and 2001, Merkel et al. (2003) found that longitudinal variability in PMC brightness was associated with the (1,1) Rossby normal mode, a westward propagating wave-1 disturbance with a period near 5 days. Von Savigny et al. (2007) found that the fluctuations in PMCs due to the five-day wave are driven by changes in temperature and not water vapor. Lower temperatures in the cold phases of the five-day wave result in more ice formation and brighter PMCs in discrete longitude sectors. Nielsen et al. (2010) found that the five-day wave can effectively prolong the PMC season. As the summer mesopause warms in the Northern Hemisphere (NH) in August and the PMCs begin to wane, zonal-mean temperatures suggest that the atmosphere is no longer saturated with respect to ice. However, as shown by Nielsen et al. (2010), a five-day wave with peak-to-peak temperature differences of less than 6 K can allow PMCs to persist in confined longitudes associated with cold wave phases.

The AIM satellite was launched on 25 April 2007 for the purpose of investigating PMCs. The present study is motivated by the anomalous nature of the 2014 NH PMC season compared with other NH seasons as observed by the AIM Cloud Imaging and Particle Size (CIPS) instrument. In particular, there was a significant and rapid decline in PMC occurrence frequencies in late July and early August of 2014 that was followed by a strong recovery before the PMC season finally ended in late August. We will show that the observed PMC variations are superficially consistent with IHC effects as discussed within the context of PMC variability observed in previous years (e.g., Karlsson, Randall, et al., 2009). However, in addition to the standard dynamical IHC mechanism as reviewed above, we propose an alternative pathway by which the IHC signal crossed the equator in 2014, namely, through an intensification of the summer easterly jet in the stratosphere and subsequent growth of the two-day wave, consistent with dynamical ideas discussed by Gu et al. (2017) for a related event in January 2006. We also present evidence that the five-day PW modulated the response of PMCs to the IHC during 2014.

## 2. Data and Analysis Method

### 2.1. CIPS

CIPS uses four wide-angle cameras to observe scattered radiation at a wavelength of 265 nm with a spatial resolution of 25 km<sup>2</sup> (McClintock et al., 2009). The CIPS PMC retrieval algorithm and a description of the level 3c data used in this work are described by Lumpe et al. (2013). CIPS cloud frequency was shown to be in good agreement with the Solar Backscatter UltraViolet (SBUV/2) instrument (Benze et al., 2009, 2011). In this work we derive PMC occurrence frequencies from the CIPS level 3c descending node data; because of the AIM orbit precession, ascending node data are not available over the entire time and latitude ranges used in this work. Frequencies are calculated on a daily basis from CIPS imagery by dividing the number of pixels identified as having cloud by the total number of pixels. The CIPS data used in this study for the years 2007–2013 correspond to Version 4.20 retrievals. The AIM orbit precession caused an increase in false detections in the NH

CIPS data beginning in 2014 because the retrieval algorithm was not designed to handle the new viewing geometries. So for 2014, the algorithm was modified to account for these errors, creating algorithm Version 5.1. Frequencies generally agree between Versions 4.20 and 5.1 to within about 10%, and the day-to-day variability is similar in both versions. Furthermore, PMC data from both the SBUV/2 and AIM Solar Occultation For Ice Experiment (SOFIE) confirm the unusual PMC behavior in 2014 (not shown).

## 2.2. Microwave Limb Sounder

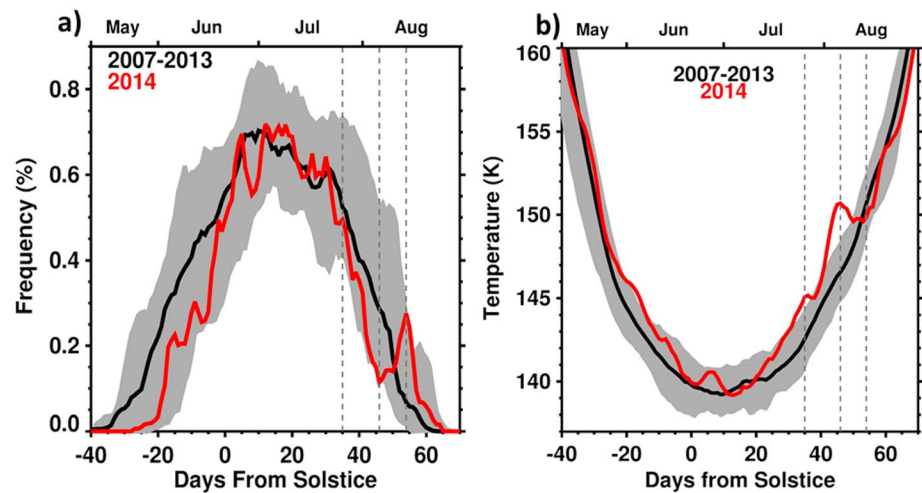
Temperature and geopotential height are derived from Version 4.2 retrievals of data from the National Aeronautics and Space Administration (NASA) Aura Microwave Limb Sounder (MLS), which provides ~3,500 vertical profiles per day between 82°S and 82°N (Livesey et al., 2017). Temperature is inferred from emission by molecular oxygen at 118 GHz. In the mesosphere between 0.01 and 0.001 hPa, temperature profiles have a vertical resolution of 8–13 km, a precision of 2.2–2.5 K, and a 4–8 K cold bias (Livesey et al., 2017). MLS geopotential height is derived from temperature and pressure and integrated from a reference geoid; it has a precision of ~45 m at 1 hPa and 110 m at 0.01 hPa (Livesey et al., 2017). We interpolate daily MLS profile data to a 2.5° latitude by 3.75° longitude grid, averaging together the gridded ascending and descending nodes to remove a large fraction of the tidal effects, to produce daily mean gridded fields. This is consistent with evidence that NH PMCs are modulated mostly by the migrating diurnal tide rather than semidiurnal tides (Stevens et al., 2017). At high latitudes MLS measures through all local times, so tides will also be effectively removed at PMC latitudes. MLS geopotential height data are used to derive daily mean geostrophic winds (e.g., Holton, 2004, Equation 3.11). Zonal mean geostrophic winds have a precision of 2 m/s at 0.01 hPa. PW amplitudes are calculated by fitting a sine wave to daily MLS geopotential height data around each latitude circle on constant pressure surfaces. The amplitude of the sine wave is considered to be the wave-1 PW (PW-1) amplitude.

## 2.3. Modern-Era Retrospective Analysis for Research and Applications, Version 2

We use winds from the Modern-Era Retrospective analysis for Research and Applications, Version 2 (MERRA-2; Gelaro et al., 2017) for stratospheric and mesospheric dynamics during 2007–2014. MERRA-2 incorporates the Goddard Earth Observing System Version 5.12.4 (GEOS-5) data assimilation system (Molod et al., 2015; Rienecker et al., 2008) and the Gridpoint Statistical Interpolation (GSI) analysis scheme (Kleist et al., 2009; Wu et al., 2002). MERRA-2 data are produced on a 0.5° latitude by 0.625° longitude grid with 72 vertical model levels from the surface to 0.01 hPa (Bosilovich et al., 2015). MERRA-2 assimilates MLS temperature data above 5 hPa to constrain the dynamics in the upper stratosphere and lower mesosphere (Fujiwara et al., 2017; Gelaro et al., 2017). This results in an improved representation of synoptic meteorological fields after August 2004.

## 2.4. NAVGEM

To study the summer mesopause temperature response to the two-day wave in 2014, we make use of a high-altitude (0–100 km) global reanalysis of the 2014 austral winter (April–October 2014) generated using a high-altitude research prototype of the Navy Global Environmental Model (NAVGEM). Eckermann et al. (2018) provide details of this NAVGEM configuration, the reanalysis experiments that were performed in 2014, and validation comparisons with other analyses and MLT observations. A unique aspect of this NAVGEM reanalysis is the unprecedented amount of observational data that was assimilated above ~50 km altitude, typically, more than  $10^5$  individual observations every 6 hr. These observations came from bias-corrected Version 4.2 MLS temperatures, Version 2.0 temperature retrievals from the Sounding of the Atmosphere using Broadband Emission Radiometry (SABER) instrument on NASA's TIMED satellite, and O<sub>2</sub> microwave radiances from the Special Sensor Microwave Imager/Sounder (SSMIS) on three separate satellites (F17, F18, and F19) of the Defense Meteorological Satellite Program. The fields used here correspond to a reanalysis run using hybrid ensemble/4DVAR (four-dimensional variational) data assimilation at a T119L74 outer-loop (T47L74 inner-loop) resolution (see Eckermann et al., 2018, for details). For the present work, these reanalyses were reinterpolated onto a pressure grid with a constant pressure-height resolution of 1 km, and from the quadratic Gaussian grid onto a regular 1° × 1° global grid. The fields are provided at a 1-hr time cadence (6-hr analysis and +1- to 5-hr outer-loop forecasts) to resolve tides in the mesosphere. As there is no comparable NAVGEM reanalysis available for other seasons, we do not use NAVGEM reanalysis fields for the comparison study.



**Figure 1.** (a) CIPS descending node PMC occurrence frequencies averaged over 70–80°N latitude versus days from solstice (DFS) for 2007–2013 (black line and gray envelope) and 2014 (red) and (b) MLS temperature averaged over 70–80°N latitude and 0.01–0.001 hPa. A 3-day running average has been applied for clarity. The vertical gray dashed lines indicate DFS 35, 46, and 54.

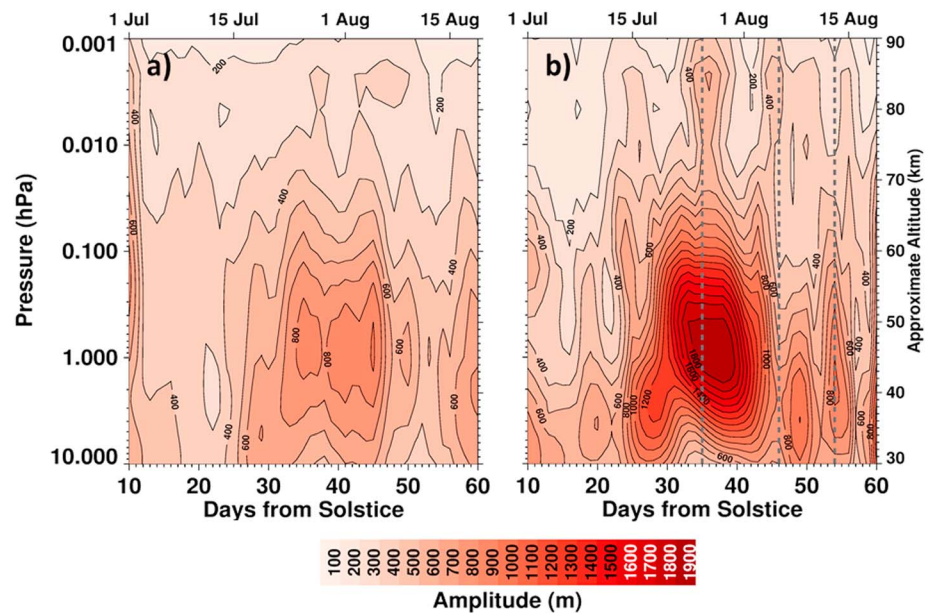
### 3. Results and Discussion

#### 3.1. IHC During 2014

CIPS PMC occurrence frequencies as a function are shown in Figure 1a of days from solstice (DFS) averaged from 70°N to 80°N for the 2007–2013 (black) and 2014 (red) NH PMC seasons. The gray envelope encompasses the range of observations (local maxima and minima) from other seasons spanning the years 2007 to 2013. In general, cloud frequencies increase rapidly at the beginning of the season, remain above ~50% for several weeks in the middle of the season, and decline to zero between DFS 60 (20 August) and 70 (30 August), consistent with previous work (e.g., Bailey et al., 2005). Here we focus on the steep decline in PMC occurrence frequency in 2014, from ~50% to ~11% between DFS 35 (26 July) and DFS 46 (6 August), followed by a recovery to ~27% by DFS 54 (14 August). The vertical dashed lines demark (from left to right) the date in 2014 that PMCs began to decline significantly below the multiyear average, the PMC occurrence frequency minimum, and the late occurrence frequency maximum. A decline in PMCs is usually associated with a corresponding increase in temperatures. Figure 1b shows the evolution of MLS temperatures averaged over 0.01–0.001 hPa and 70°N–80°N. Consistent with Figure 1a, temperatures increase to ~150.5 K on DFS 46, 4 K higher than the 2007–2013 mean on that day. Temperatures then decline between about DFS 46 and 54, consistent with the late increase in PMC occurrence frequency.

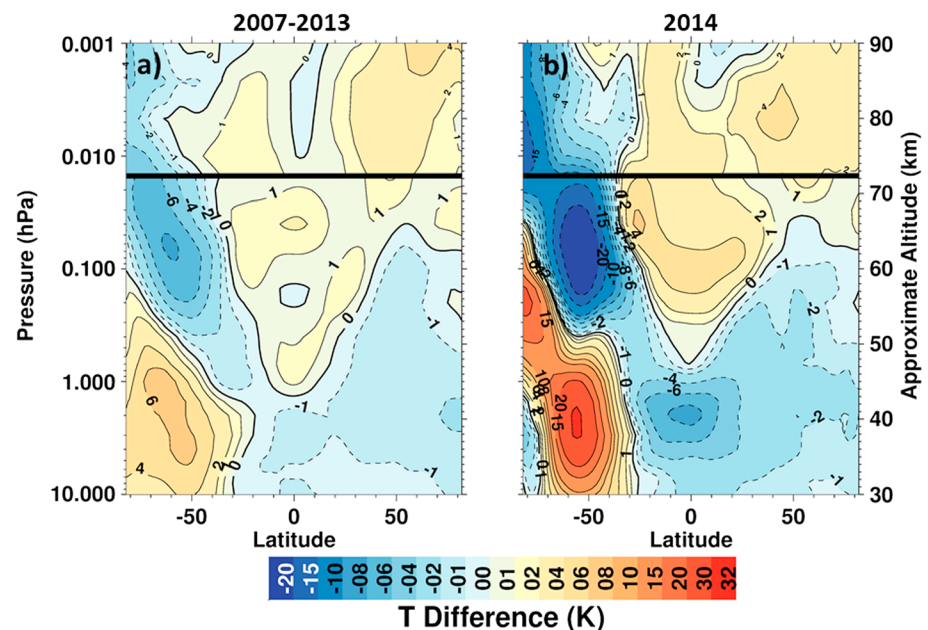
In order to explain this atypical evolution of PMC occurrence frequencies in late July and early August of 2014, we first consider the possible contribution of IHC. As described above, according to the conventional IHC mechanism, large-amplitude PWs in the winter hemisphere can lead to warming at the summer mesopause. Figure 2 shows daily PW-1 amplitudes at 60°S and between 10 and 0.001 hPa, based on MLS geopotential height for (a) 2007–2013 and (b) 2014. PW activity in the midlatitude Southern Hemisphere (SH) is generally weak throughout the northern PMC season during 2007–2013, with PW-1 amplitudes ranging from about 200 to 800 m, and a maximum of ~900 m near 10 hPa. In 2014 SH PW-1 amplitudes increase rapidly near DFS 22 and reach a maximum of 1,900 m at 1.0 hPa on DFS 36, 10 days before the minimum in NH PMC occurrence frequencies. These results are broadly consistent with detailed studies of stratospheric dynamics during the austral winter of 2014 using both MLS data and reanalysis reported by Gisinger et al. (2017). They showed that this enhanced quasi-stationary PW-1 activity near 60°S dissipated in the upper stratosphere, leading to Eliassen-Palm flux divergence (EPFD) that weakened the winter stratospheric jet and drove a zonal-mean warming from 1 to 10 hPa of up to 7 K relative to climatological conditions in July and August, a prerequisite for IHC. Although this alone is not definitive proof, these findings and the results in Figure 2 are consistent with IHC as a causal mechanism for the observed decline in NH PMCs from DFS 35 to 46 in 2014.



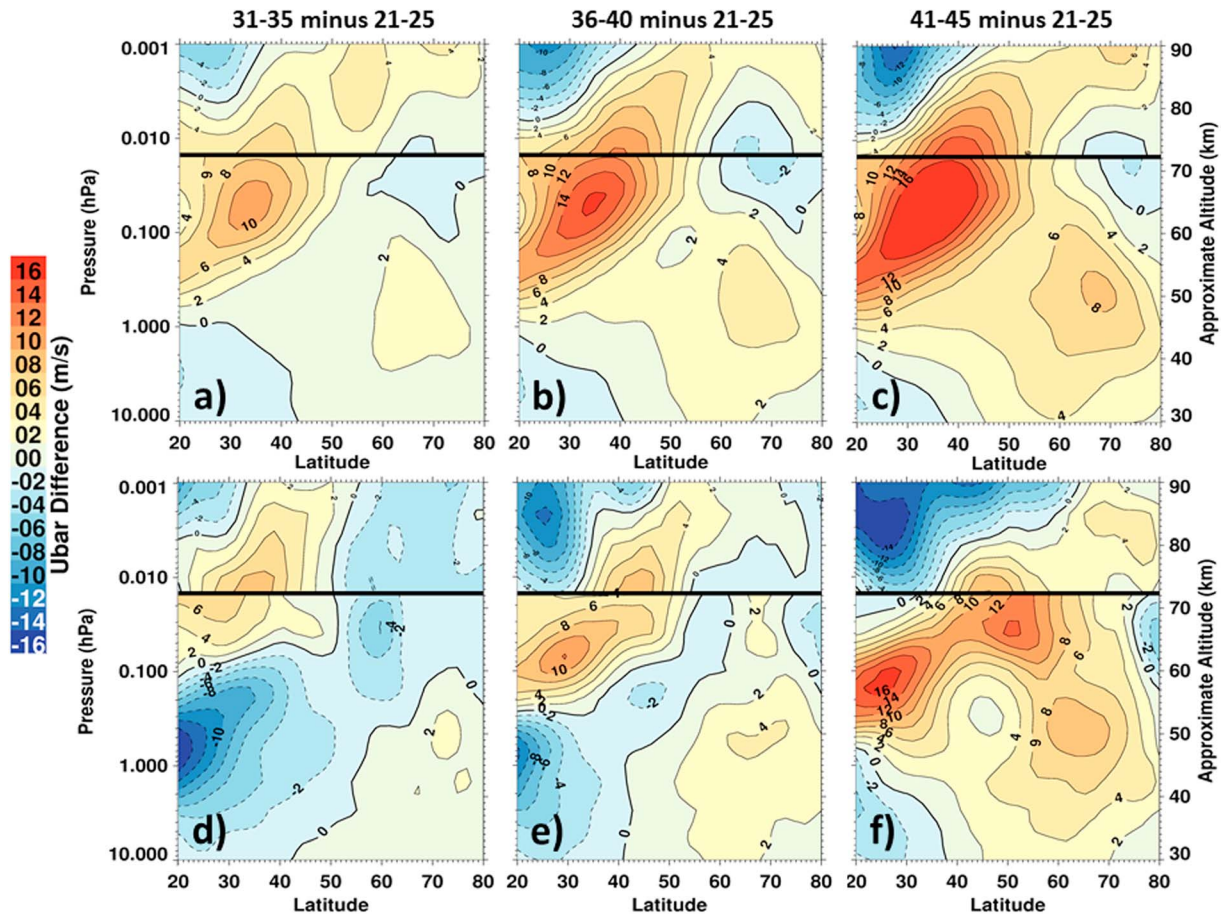


**Figure 2.** Planetary wave-1 amplitudes at 60°S as a function of pressure and time for (a) 2007–2013 and (b) 2014. Vertical gray dashed lines indicate DFS 35, 46, and 54.

To explore the mechanism further, Figures 3 and 4 compare key diagnostics of IHC in the temperature and wind fields of 2007–2013 and 2014. A quadrupole pattern in zonal-mean temperature anomalies, characterized by warming in the polar winter stratosphere and equatorial mesosphere and cooling in the polar winter mesosphere and equatorial stratosphere, is typically associated with enhanced wintertime PW breaking (e.g., Andrews et al., 1987). To illustrate this, the period just prior to the growth of the PWs (DFS 21–25) is subtracted from the period near the peak of the PWs (DFS 31–35). Figure 3a shows the average difference during 2007–2013. Although the climatological quadrupole pattern shown in Figure 3a is evident, the low-latitude temperature anomalies are generally less than 1 K. In 2014, on the other hand, there is a strong quadrupole



**Figure 3.** Zonal mean MLS temperature for DFS 31–35 minus zonal mean MLS temperature for DFS 21–25 during (a) 2007–2013 and (b) 2014. Note the nonlinear color scale to emphasize small temperature differences.



**Figure 4.** Zonal mean zonal wind change between DFS 21–25 and (a and d) 31–35, (b and e) 36–40, and (c and f) 41–45 during (a–c) 2007–2013 and (d–f) 2014. Winds are based on MERRA-2 below 0.015 hPa and MLS geostrophic winds above 0.015 hPa, delineated by the thick black line.

structure, with low-latitude temperature anomalies of  $\sim 2$ – $6$  K in the mesosphere and  $\sim 4$ – $8$  K in the stratosphere. Gisinger et al. (2017) report similar anomalies in 2014 zonal-mean reanalysis temperatures relative to a 36-year climatological mean. The temperature shift in 2014 is consistent with PW-1 EPFD-induced deceleration of the zonal mean winter stratosphere westerlies, which drive an observed high-latitude warming below 45 km (Gisinger et al., 2017) and, through an associated anomalous residual circulation, the low-latitude cooling in the same altitude region. This zonal wind deceleration also would have altered the vertical propagation and filtering of nonorographic GWs through the stratosphere into the mesosphere, leading to a weakened mesospheric residual circulation and the observed high-latitude cooling and low-latitude warming. That is, weakening of the mesospheric residual circulation leads to less descent and thus less adiabatic warming in the polar winter mesosphere; and as explained above, the weakened circulation also causes adiabatic warming in the equatorial lower mesosphere.

According to thermal wind arguments, warming in the equatorial and subtropical mesosphere should induce a westerly zonal-mean zonal wind anomaly in the midlatitude summer mesosphere. Previous work argues that this westerly wind anomaly would lower the breaking altitudes of GWs with eastward phase speeds, preventing them from propagating up to the mesopause (e.g., Figure 2 in Körnich & Becker, 2010).

To understand how the observed temperature shift in 2014 changed the NH winds, Figure 4 shows the zonal-mean zonal wind for DFS 31–35, 35–40, and 41–45 minus DFS 21–25 during 2007–2013 (Figures 4a–4c) and 2014 (Figures 4d–4f). MERRA-2 winds are used below 0.015 hPa, and MLS geostrophic winds are used above 0.015 hPa. Equatorward of  $20^{\circ}\text{N}$ , zonal wind tendencies are dependent on the tropical semiannual oscillation and quasi-biennial oscillation, and thus are not shown. DFS 21–25 was chosen as this is just prior to the period of enhanced SH PW activity in 2014, while DFS 31–35, 36–40, and 41–45 occur right before the

decline in PMCs, during the beginning of the decline in PMCs, and at the end of the decline in PMCs, respectively.

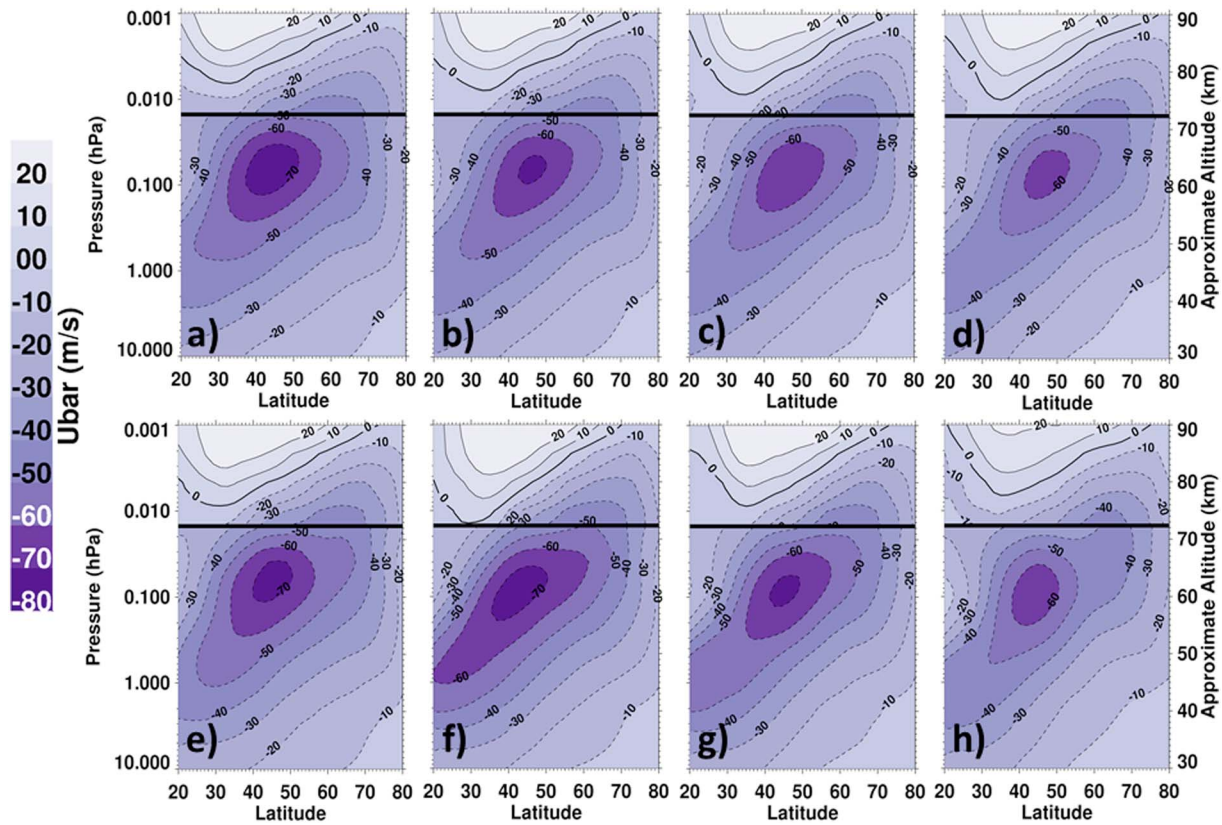
During 2007–2013, the wind shift is dominated by a weakening of the summer easterly jet, with the jet core weakening by  $\sim 1 \text{ m} \cdot \text{s}^{-1} \cdot \text{day}^{-1}$  throughout the period from DFS 31 to 45. In 2014, the zonal mean zonal wind exhibits a westerly shift of 2–8 m/s in the low-latitude upper mesosphere near 0.01 hPa between DFS 21–25 and DFS 31–35, consistent with a thermal wind adjustment to the warming of the equatorial mesosphere near 0.1 hPa shown in Figure 3b. However, a westerly shift of 2–6 m/s was also observed during 2007–2013 in this region. Following DFS 31–35, the westerly shift in 2014 becomes weaker than in the 2007–2013 average throughout the mesosphere. It is possible that the westerly wind shift in 2014 of 2–8 m/s between DFS 21–25 and DFS 31–35 was at least partially due to the low-latitude mesospheric warming shown in Figure 3b, that is, conventional IHC, though the shift is only slightly greater than that of the multiyear mean.

While the subtropical zonal wind anomaly in the mesosphere in 2014 is not sufficient to explain the anomalous decline in PMCs, there is also a 4–15 m/s easterly anomaly in the upper stratosphere and lower mesosphere (USLM,  $\sim 50$ –60 km) between  $20^\circ\text{N}$  and  $40^\circ\text{N}$ , shown in Figure 4d. This occurs near the equatorward flank of the easterly jet core (e.g., Randel et al., 2004). During 2007–2013, the easterly jet in the USLM was weakening during this time, consistent with the seasonal cycle. Strengthening of the summer easterlies following enhanced wintertime PW activity is consistent with results from a 19-year simulation of the Canadian Middle Atmosphere Model by Karlsson, McLandress, and Shepherd (2009), who found strengthening easterlies at midlatitudes below 75 km that were attributed to the effect of the enhanced subtropical temperature gradient due to the equatorial stratospheric cooling. Similarly, Gu et al. (2017) found a strengthening of the summer easterlies in the SH during 2006 following a stratospheric sudden warming in the NH. This easterly anomaly in 2014 persists in the USLM through DFS 36–40 before rapidly weakening, consistent with the seasonal cycle.

To further understand the evolution of the winds, Figure 5 shows the zonal mean zonal winds in MERRA-2 (below 0.015 hPa) and MLS geostrophic winds (above 0.015 hPa) from  $20^\circ\text{N}$  to the pole for DFS 21–25, 31–35, 35–40, and 41–45 for 2007–2013 (Figures 5a–5d) and 2014 (Figures 5e–5h). Consistent with Figure 4, the most notable shift during 2007–2013 is a weakening of the easterly jet from  $\sim 75$  to 60 m/s between DFS 21 and 45. During 2014, the easterly jet strengthens between DFS 21–25 and 31–35, particularly along the equatorward flank, with easterly winds of 60 m/s extending to  $20^\circ\text{N}$ . In 2014, the easterly jet weakens, consistent with climatology, between DFS 31–35 and 41–45. It is worth noting that in 2014 the zero wind line near  $30^\circ\text{N}$  and 0.01 hPa is  $\sim 4$  km lower on DFS 31–35 than on DFS 21–25; it is also lower than the average in 2007–2013 on DFS 31–35. This indicates a downward shift in westerly winds and the filtering of eastward propagating GWs (e.g., Karlsson, McLandress, & Shepherd, 2009). The zero wind line shifts up in altitude on DFS 36–40, becoming higher in altitude than the 2007–2013 mean by DFS 41–46. The downward shift during DFS 31–35 is consistent with conventional IHC and likely weakened the residual circulation through modified wave filtering, leading to the warming that occurred prior to DFS 36 (see Figure 1b) contributing to and the anomalous decline in PMCs associated with the second period of warming between DFS 38 and 46. Often there is a lag in conventional IHC between wintertime PWs and the decline in PMCs of up to 10 days. Had conventional IHC produced the warming that occurred following DFS 37, however, we would expect the westerly shift in the upper-mesosphere winds to persist throughout the period, since this is what drives the change in mesospheric GW filtering and subsequent weakening of the residual circulation. It is possible, given the observed evolution of the mesospheric winds, that conventional IHC led to the initial decline in PMCs prior to DFS 38 and preconditioned the PMC region for the sharp decline in PMCs in response to the warming between DFS 38 and 46.

The net effect of the  $\sim 5$ –10 m/s easterly wind anomaly in the USLM and the 2–8 m/s westerly anomaly above 65 km is to significantly enhance the meridional and vertical gradients in the zonal wind along the equatorward flank of the summer easterly jet, shown in Figure 5f. These in turn contribute to a negative meridional gradient in the zonal mean potential vorticity (PV), which is a requirement for baroclinic instability and PW growth (e.g., Andrews et al., 1987; Holton, 2004; McCormack et al., 2014; Nielsen et al., 2010). Analysis of NAVGEM winds reveals a similar strengthening of the easterly jet in 2014 and a coincident increase in Eliassen-Palm-flux divergence along the equatorward flank of the jet, between about  $25^\circ\text{N}$  and  $45^\circ\text{N}$  and 55 and 65 km, with values  $> 20 \text{ m} \cdot \text{s}^{-1} \cdot \text{day}^{-1}$  between DFS 33 and 47 (not shown). Previous work has





**Figure 5.** Zonal mean zonal wind for (a and e) DFS 21–25, (b and f) DFS 31–35, (c and g) DFS 36–40, and (d and h) DFS 41–46 for (a–d) 2007–2013 and (e–h) 2014. Winds are based on MERRA-2 below 0.015 hPa and MLS geostrophic winds above 0.015 hPa, delineated by the thick black line.

shown that the quasi-two-day wave often emerges from such baroclinically unstable regions, which typically peak near solstice when the easterly jet and resulting shears are strong (e.g., McCormack et al., 2014; Salby & Callaghan, 2001). Gu et al. (2016; 2017) found that two-day wave amplification occurs through instabilities of the mean flow associated with the summer easterly jet. The two-day wave in the summer mesosphere is relevant to the occurrence of PMCs, as it can lead to a warming of the polar mesopause region by producing westward drag in the summer mesosphere, which counters the GW drag driving the residual circulation, leading to reductions in residual meridional and vertical velocities (Lieberman, 1999, 2002; Pendlebury, 2012; Siskind & McCormack, 2014).

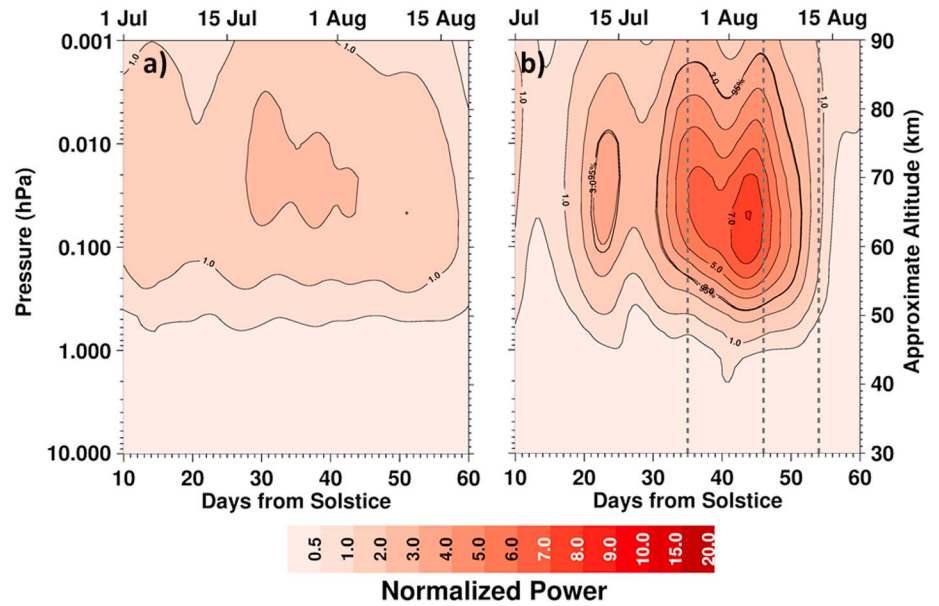
The properties of the two-day wave are investigated in 2007–2013 and 2014 using a Morlet wavelet analysis (Torrence & Compo, 1998). This method is used to identify periodic behavior in MLS geopotential height at each grid point around the 30°N latitude circle, with a band pass of 2–2.4 days. The 95% confidence level is determined using a chi-square test compared to a white noise null hypothesis, following the method of Torrence and Compo (1998). Figure 6 shows the normalized geopotential-height amplitude of the two-day wave at 30°N for 2007–2013 (Figure 6a) and 2014 (Figure 6b). Figure 6b shows a large two-day wave occurring throughout the mesosphere between DFS 31 and 52 in 2014, with a peak near DFS 44, consistent with the findings of Pancheva et al. (2017), who found enhanced two-day wave amplitudes in 2014 centered at ~35°N, based on MLS data. Two-day wave activity is generally weak during 2007–2013.

The influence of the two-day wave upon the mean flow in 2014 is determined using the quasi-geostrophic version of the transformed Eulerian mean (TEM) equations governing the zonally averaged wind and temperature, given by

$$\bar{u}_t - f_0 \bar{v}^* - \bar{\chi} = \rho_0^{-1} \nabla \cdot \mathbf{F} \quad (1)$$

$$\bar{\Theta}_t + \bar{w}^* \Theta_{0z} - \bar{Q} = 0 \quad (2)$$





**Figure 6.** Normalized two-day wave amplitude derived from MLS geopotential height at 30°N as a function of pressure and time during (a) 2007–2013 and (b) 2014. The amplitude is normalized by the variance of the detrended geopotential height data (detrended by subtracting the 31-day running mean) around the 30°N latitude circle. The vertical gray dashed lines indicate DFS 35, 46, and 54. The 95% contour indicates the region where the two-day wave is statistically significant at the 95% confidence level.

$$(a \cos \phi)^{-1} (\bar{v}^* \cos \phi)_\phi + \rho_0^{-1} (\rho_0 \bar{w}^*)_z = 0 \quad (3)$$

$$f \bar{u} + a^{-1} \bar{\Phi}_\phi = 0 \quad (4)$$

(Andrews et al., 1987).  $\bar{v}^*$  and  $\bar{w}^*$  are the residual mean meridional and vertical winds, respectively. They are related to the their Eulerian counterparts  $\bar{v}$  and  $\bar{w}$  by

$$\bar{v}^* = \bar{v} - \rho_0^{-1} \left( \rho_0 \bar{v}' \bar{\theta}' / \Theta_{0z} \right)_z \quad (5)$$

$$\bar{w}^* = \bar{w} + \left( \bar{v}' \bar{\theta}' / \Theta_{0z} \right)_y \quad (6)$$

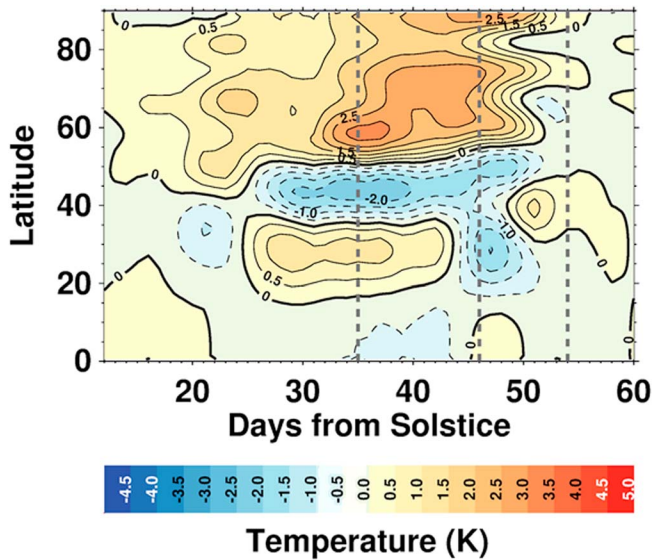
$\phi$  denotes latitude,  $\Phi$  is geopotential,  $Q$  is the net diabatic heating rate,  $\bar{X}$  is GW drag,  $f_0$  is the Coriolis parameter,  $a$  is the radius of the Earth, and  $\Theta$  is the potential temperature. While  $\bar{\Theta}$  denotes the zonally averaged potential temperature,  $\bar{\Theta}_0$  refers to a global reference potential temperature profile that varies only in the vertical.

The vector  $\mathbf{F}$  is known as the Eliassen-Palm flux and is defined as

$$\mathbf{F} = \left( 0, -\rho_0 \bar{v}' \bar{u}', \rho_0 f_0 \bar{v}' \bar{\theta}' / \Theta_{0z} \right) \quad (7)$$

$\mathbf{F}$  depicts the transfer of “wave action” density (defined as  $\bar{\Theta} \frac{1}{2} \rho_0 \bar{q}'^2 / \bar{q}_y$  for quasigeostrophic waves) from one latitude or altitude to another. The divergence of  $\mathbf{F}$  per unit mass ( $\rho_0^{-1} \nabla \cdot \mathbf{F}$ ) represents the zonal force upon the mean flow.

The response of the zonal mean wind and temperature to the two-day wave is examined quantitatively using a linear, quasi-geostrophic model of the TEM circulation formulated by Garcia (1987). Gravity-wave drag  $\bar{X}$  is represented as Rayleigh friction, and the net diabatic heating  $\bar{Q}$  is given by the sum of shortwave heating and Newtonian cooling. The Rayleigh coefficient  $K_R$  is set to 1 day<sup>−1</sup>, which is the most conservative (i.e.,



**Figure 7.** Two-day wave-driven temperature based on NAVGEM data at  $\sim 80$  km, in 2014. The vertical gray dashed lines indicate DFS 35, 46, and 54.

slowest) value inferred by Lieberman et al. (2010) from mesospheric and lower thermospheric winds and temperatures. The Newtonian relaxation  $\alpha$  is set to  $0.5 \text{ day}^{-1}$  in order to maintain a  $K_R/\alpha$  ratio of 2 that produced the most realistic zonal wind structures in the experiments of Garcia (1987).

The two-day wave driving and vertical heat flux divergence per unit mass are treated as steady state quantities and expanded in the form

$$\rho_0^{-1} \nabla \cdot \mathbf{F} \equiv \bar{M}(\mu, z) = \sum_n M_n(z) \mu B_n(\mu) \quad (8)$$

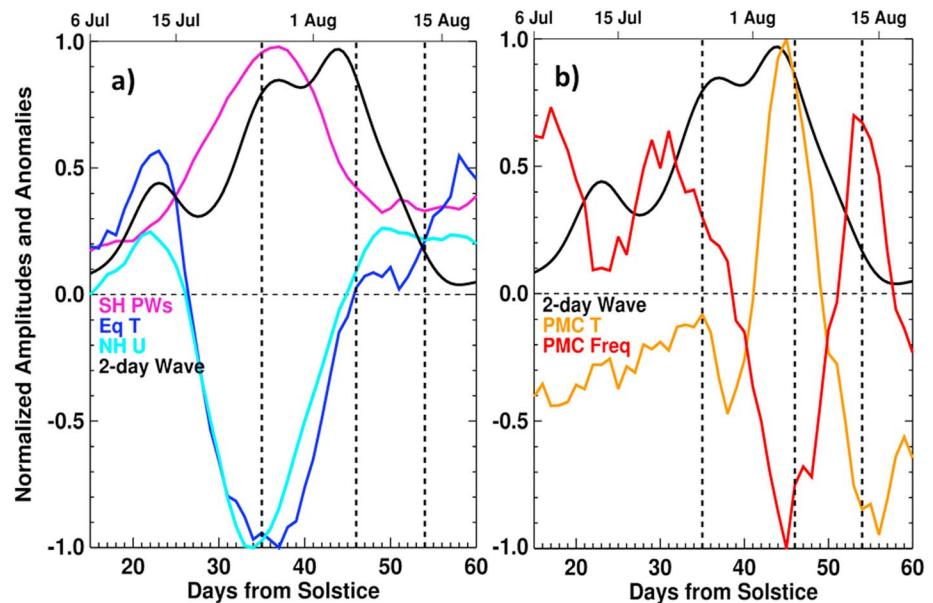
$$\rho_0^{-1} \left[ \rho_0 f_0 v' \theta' / \Theta_{0z} \right]_z \equiv \bar{M}_H(\mu, z) = \sum_n M_{Hn}(z) \mu B_n(\mu) \quad (9)$$

Here  $\mu = \sin \phi$  and  $B_n(\mu)$  are the latitudinal eigenfunctions of the mass streamfunction  $\chi$ . Plumb (1982) showed that these are related to the Hough functions  $H_n(\mu)$  of Laplace's tidal equation for steady, zonally averaged flow according to

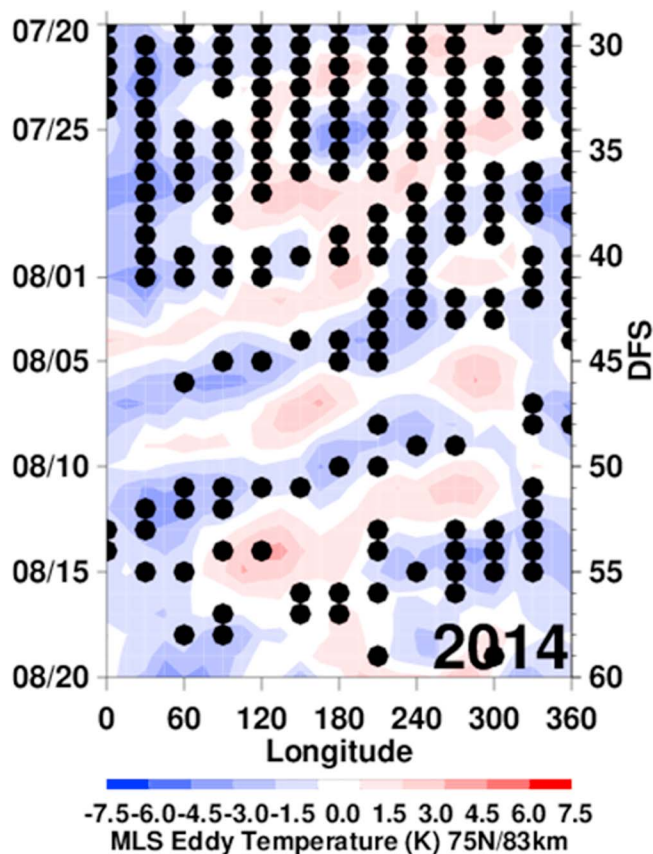
$$H_n(\mu) = \frac{d}{d\mu} \left[ B_n(\mu) (1 - \mu^2)^{1/2} \right] \quad (10)$$

Hourly NAVGEM data are used to compute the two-day wave-driving terms every 6 hr, and the resulting summer mesopause temperature

response to the two-day wave in 2014 is shown in Figure 7. The two-day wave generally leads to cooling at latitudes equatorward of  $\sim 50^\circ\text{N}$  and warming poleward of  $50^\circ\text{N}$ , due to meridional winds associated with the two-day wave, driving high temperatures poleward and low temperatures equatorward. In the PMC region, the two-day wave drives an  $\sim 2$ – $3$  K increase in temperature, consistent with a weakened residual circulation. The timing and amplitude of the two-day wave-driven temperature anomaly is consistent with the atypical decline in PMCs during 2014.



**Figure 8.** Time series of MLS geopotential height PW-1 at  $60^\circ\text{S}$  and 1 hPa (purple); MLS temperature at  $5^\circ\text{S}$  to  $5^\circ\text{N}$  and 10 hPa, minus the 30-day running mean (dark blue); MERRA-2 zonal wind averaged between  $20^\circ\text{N}$  and  $30^\circ\text{N}$  at 1 hPa, minus the 30-day running mean (light blue); MLS geopotential height two-day wave amplitude at  $30^\circ\text{N}$  averaged between 0.1 and 0.01 hPa (black); MLS temperature at  $70^\circ\text{N}$  and  $80^\circ\text{N}$  minus the 30-day running mean (orange); and CIPS PMC frequencies between  $70^\circ\text{N}$  and  $80^\circ\text{N}$  minus the 30-day running mean (red). Each time series is normalized by the maximum absolute value between DFS 10 and DFS 60. The vertical gray dashed lines indicate DFS 35, 46, and 54.



**Figure 9.** Longitude-time Hovmöller plot of MLS eddy temperature at ~83 km and 75°N for DFS 29–60. The black dots indicate where PMCs are present 40% of the time in each 30° longitude bin.

To summarize the temporal evolution of the IHC, two-day wave growth, and decline in PMCs in 2014, we show time series of the relevant processes discussed above in Figure 8. Specifically, Figure 8a shows time series of SH PW amplitudes (purple), equatorial zonal-mean temperature anomalies (dark blue), subtropical summer stratospheric zonal wind anomalies (light blue), and summer mesospheric two-day wave amplitudes (black). Figure 8b shows time series of summer mesospheric two-day wave amplitudes (black; repeated for context), summer polar mesopause zonal-mean temperature anomalies (orange), and PMC frequency anomaly (red). The PWs are normalized with respect to the maximum wave amplitude between DFS 10 and 60. The 30-day running mean is subtracted from temperature, zonal wind, and PMC frequency to remove the late-summer seasonal cycle. These are also normalized by their respective maximum anomaly. The first step in the evolution is the growth in SH PW-1 amplitudes (purple), which led to EPFD and warming in the extratropical SH winter stratosphere (Gisinger et al., 2017). As discussed above, this wave forcing intensified the residual circulation that led to the stratospheric equatorial cooling (dark blue), resulting in an equatorial temperature minimum on DFS 36. The stratospheric cooling modified the extratropical summer stratospheric temperature gradient, leading to the observed strengthening of the summer easterly jet in 2014 (light blue) between about DFS 25 and 34. The resulting enhancement of the mesospheric summer easterly jet leads to enhanced shear and baroclinic instability along the equatorward flank of the jet and in situ growth of the two-day wave (black), which grows rapidly between DFS 30 and DFS 37. The two-day wave amplitudes peak on DFS 44, and EPFD of this wave yields a westward drag anomaly that weakens the residual circulation, driving the coincident peak in polar summer mesopause temperature anomaly (orange) and minimum in PMC frequency (red).

### 3.2. Five-Day Wave Effects on PMCs During 2014

While the general decline of PMCs in response to the two-day wave-driven warming is consistent with previous work, the regional evolution of PMCs during the warming is complicated by the presence of a large five-day PW-1 ([1,1] Rossby normal mode) in the polar summer mesopause region. The five-day wave in 2014 is driven by baroclinic instability arising from a negative meridional gradient in PV, similar to the two-day wave discussed above. Consistent with the findings of Nielsen et al. (2010), who considered the growth of the five-day wave during the 2007 northern summer, the enhanced vertical and meridional gradient in the zonal mean zonal wind near 30–50°N and 0.1–0.01 hPa during DFS 31–35 (see Figure 4f) led to a negative meridional gradient in PV of about  $-10^{-10} \cdot \text{m}^{-1} \cdot \text{s}^{-1}$  near 0.01 hPa between 30°N and 50°N (not shown). As discussed above, this leads to baroclinic instability and PW growth.

Figure 9 shows a longitude-time Hovmöller diagram of MLS eddy temperature (deviation from the daily zonal mean) at 75°N and 83 km from DFS 29 to DFS 60 (20 July to 20 August) in 2014. The black dots indicate daily PMC occurrence frequencies greater than 40% in each 30° longitude bin. A five-day PW-1 is evident in the MLS temperature anomalies throughout the monthlong time period. PMC occurrence frequencies were >40% in both the warm and cold phases during the relatively cool period prior to DFS 35 (26 July). With the two-day wave-driven temperature increase in the PMC region, PMCs were able to persist only in the coldest wave phases. Thus, without this five-day PW-1, PMC occurrence frequencies would likely have declined even more during the IHC-induced warming in 2014. That is, the five-day PW-1 enhanced the PMC frequencies in August of 2014, consistent with a similar effect in the 2007 NH PMC season reported by Nielsen et al. (2010).

The zonal-mean temperature in the PMC region in 2014 decreased by ~1 K from DFS 46 to 54 (see Figure 1b) as the atmosphere recovered from the IHC-induced warming, causing PMC occurrence frequencies to increase from 11% to 27% (the temperature decrease and PMC increase are both shown as normalized

anomalies in Figure 8, and the absolute PMC increase is shown in Figure 1). During this same period in the 2007–2013 mean, temperatures increased by 4 K in accordance with the seasonal cycle, with a corresponding decrease in PMCs from ~28% to ~6%. Figure 9 suggests that by DFS 54 the average temperature in 2014 had decreased enough that PMCs were present at times even in the warm phases of the five-day wave. Had five-day wave amplitudes been weaker, the PMC increase during the recovery from IHC might have been even greater. After DFS 54 in 2014 the zonal-mean temperature increased and the five-day wave amplitude weakened from ~3–4 K to ~1 K, resulting in a rapid decline of PMC occurrence frequencies at the end of the season.

#### 4. Summary and Conclusions

PMC occurrence frequencies derived from AIM CIPS measurements in the NH summer of 2014 exhibited an anomalous decline of ~80% from 26 July to 6 August. Using MLS temperatures and derived geostrophic wind and PW activity, MERRA-2 reanalysis winds, and a quasi-geostrophic model of two-day -wave dynamics driven by high-altitude NAVGEM reanalysis fields, we argue that this anomalous decline in PMCs can be attributed to IHC-driven growth of the two-day wave. Our results indicate that strong quasi-stationary PW-1 activity in the 2014 extratropical SH (winter) stratosphere led to wave breaking (Gisinger et al., 2017) that in turn drove a quadrupole pattern in zonal-mean temperature anomalies relative to the 2007–2013 mean. In agreement with previous work and wave-mean flow concepts, we conclude that changes in latitudinal temperature gradients caused by the PW activity led to zonal-mean anomalies in zonal winds in both the extratropical SH and subtropical NH. In contrast to results of previous IHC studies, however, we conclude that in 2014 the IHC impact on summer polar mesopause temperatures and PMCs was triggered predominantly by the growth of the two-day wave. Which in turn was triggered by enhanced shear of the zonal wind, driven primarily by a strengthening of the easterly jet in the NH upper stratosphere and lower mesosphere, led to a baroclinically unstable atmosphere and subsequent growth of the midlatitude two-day wave. Consistent with previous work, the two-day wave deposits westward momentum in the mesosphere, weakening the summertime mesospheric residual circulation, and warming the polar mesopause region. We contend that conventional IHC played a secondary role in the decline of PMCs in 2014, through warming the PMC region ~2 weeks prior to the minimum in PMCs, preconditioning the PMC region such that the two-day wave-driven warming led to a more rapid decline in PMCs.

The analysis also shows that late-season PMCs were affected by the five-day PW-1 ([1,1] Rossby normal mode) in 2014. The IHC-induced decline would likely have been even larger, were it not for a strong five-day wave that allowed PMCs to persist in the cold phases of the wave even though the zonal mean temperature had increased. PMC occurrence frequencies recovered from the warming within a week, as the zonal mean temperature dropped by ~1 K during a time when the 2007–2013 mean temperature increased by 4 K. The recovery may have been even faster or more extensive, but the five-day wave limited PMC formation in the warm wave phases. This work emphasizes the simultaneous impacts of IHC, the two-day PW, and the five-day PW on PMCs.

#### References

- Andrews, D. G., Holton, J. R., & Leovy, C. B. (1987). *Middle atmosphere dynamics* (1st ed.). San Diego, CA: Academic Press.
- Bailey, S. M., Merkel, A. W., Thomas, G. E., & Carstens, J. N. (2005). Observations of polar mesospheric clouds by the Student Nitric Oxide Explorer. *Journal of Geophysical Research*, 110, D13203. <https://doi.org/10.1029/2004JD005422>
- Becker, E., & Fritts, D. C. (2006). Enhanced gravity-wave activity and interhemispheric coupling during the MacWAVE/MIDAS northern summer program 2002. *Annales de Geophysique*, 24(4), 1175–1188. <https://doi.org/10.5194/angeo-24-1175-2006>
- Becker, E., Müllemann, A., Lübken, F.-J., Körnich, H., Hoffmann, P., & Rapp, M. (2004). High Rossby-wave activity in austral winter 2002: Modulation of the general circulation of the MLT during the MacWAVE/MIDAS northern summer program. *Geophysical Research Letters*, 31, L24503. <https://doi.org/10.1029/2004GL019615>
- Becker, E., & Schmitz, G. (2003). Climatological effects of orography and land-sea heating contrasts on the gravity-wave driven circulation of the mesosphere. *Journal of the Atmospheric Sciences*, 60(1), 103–118. [https://doi.org/10.1175/1520-0469\(2003\)060%3C0103:CEOAL%3E2.0.CO;2](https://doi.org/10.1175/1520-0469(2003)060%3C0103:CEOAL%3E2.0.CO;2)
- Benze, S., Randall, C. E., DeLand, M. T., Thomas, G. E., Bailey, S. M., Russell, J. M. III, & Merkel, A. W. (2011). Evaluation of AIM CIPS measurements of polar mesospheric clouds by comparison with SBUV data. *Journal of Atmospheric and Solar-Terrestrial Physics*, 73(14–15), 2065–2072. <https://doi.org/10.1016/j.jastp.2011.02.003>
- Benze, S., Randall, C. E., DeLand, M. T., Thomas, G. E., Rusch, D. W., Bailey, S. M., et al. (2009). Comparison of polar mesospheric cloud measurements from the cloud imaging and particle size experiment and the solar backscatter ultraviolet instrument in 2007. *Journal of Atmospheric and Solar - Terrestrial Physics*, 71(3–4), 365–372. <https://doi.org/10.1016/j.jastp.2008.07.014>

#### Acknowledgments

This work was supported by the NASA Small Explorer Program through contract NAS5-03132 and through the NASA Heliophysics Guest Investigator grant 80NSSC18K0051. NRL authors acknowledge generous support of the Chief of Naval Research via the base 6.1, 6.2, and platform support programs. V. L. H. was supported by NSF CEDAR grant 1343031 and NASA HGI grant NNX17AB80G. S. D. E. acknowledges support for NAVGEM runs from the DoD High Performance Computer Modernization Program via grants of computer time at the Navy DoD Supercomputing Resource Center. CIPS level 3c summary files and software for reading the files are available at <http://lasp.colorado.edu/aim>. We thank the CIPS data processing team and AIM mission operations team for their exceptional contributions. MLS v4.2 data are available from the NASA Goddard Space Flight Center Earth Sciences (GES) Data and Information Services Center (DISC) at <https://mls.jpl.nasa.gov/data/>. MERRA-2 data are available at MDISC, managed by the NASA GES DISC at <https://gmao.gsfc.nasa.gov/reanalysis/MERRA-2/>. The quasi-geostrophic model output of two-day wave forcing is available through Open Science Framework at <https://osf.io/4hky3/>. J. A. F. and R. S. L. wish to dedicate this paper to the memory of Brian Laughman.



- Bosilovich, M. G., Akella, S., Coy, L., Cullather, R., Draper, C., Gelaro, R., et al. (2015). *MERRA-2: Initial evaluation of the climate, NASA Tech. Rep. Series on Global Modeling and Data Assimilation, NASA/TM-2015-104606* (Vol. 43). Greenbelt, MD: NASA Goddard Space Flight Center.
- de Wit, R. J., Hibbins, R. E., Espy, P. J., & Hennum, E. A. (2015). Coupling in the middle atmosphere related to the 2013 major sudden stratospheric warming. *Annales de Geophysique*, 33(3), 309–319. <https://doi.org/10.5194/angeo-33-309-2015>
- Eckermann, S. D., Ma, J., Hoppel, K. W., Kuhl, D. D., Allen, D. R., Doyle, J. A., et al. (2018). High-altitude (0–100 km) global atmospheric reanalysis system: Description and application to the 2014 austral winter of the Deep Propagating Gravity-Wave Experiment (DEEPWAVE). *Monthly Weather Review*. <https://doi.org/10.1175/MWR-D-17-0386.1>
- Fujiwara, M., Wright, J. S., Manney, G. L., Gray, L. J., Anstey, J., Birner, T., et al. (2017). Introduction to the SPARC Reanalysis Intercomparison Project (S-RIP) and overview of the reanalysis systems. *Atmospheric Chemistry and Physics*, 17(2), 1417–1452. <https://doi.org/10.5194/acp-17-1417-2017>
- Garcia, R. R. (1987). On the mean meridional circulation of the middle atmosphere. *Journal of the Atmospheric Sciences*, 44(24), 3599–3609. [https://doi.org/10.1175/1520-0469\(1987\)044%3C3599:OTMMCO%3E2.0.CO;2](https://doi.org/10.1175/1520-0469(1987)044%3C3599:OTMMCO%3E2.0.CO;2)
- Gelaro, R., McCarty, W., Suarez, M. J., Todling, R., Molod, A., Takacs, L., et al. (2017). The Modern-Era Retrospective Analysis for Research and Applications, Version 2 (MERRA-2). *Journal of Climate*, 30(14), 5419–5454. <https://doi.org/10.1175/JCLI-D-16-0758.1>
- Gisinger, S., Dornbrack, A., Mathias, V., Doyle, J. D., Eckermann, S. D., Ehard, B., et al. (2017). Atmospheric conditions during the Deep Propagating Gravity Wave Experiment (DEEPWAVE). *Monthly Weather Review*, 145(10), 4249–4275. <https://doi.org/10.1175/MWR-D-16-0435.1>
- Gu, S.-Y., Dou, X., & Pancheva, D. (2017). Investigation on the abnormal quasi-two day wave activities during sudden stratospheric warming period of January 2006. *Atmospheric Chemistry and Physics Discussions*, 1–37. <https://doi.org/10.5194/acp-2017-563>
- Gu, S.-Y., Liu, H. L., Dou, X., & Li, T. (2016). Influence of the sudden stratospheric warming on quasi-2-day waves. *Atmospheric Chemistry and Physics*, 16(8), 4885–4896. <https://doi.org/10.5194/acp-16-4885-2016>
- Gumbel, J., & Karlsson, B. (2011). Intra- and inter-hemispheric coupling effects on the polar summer mesosphere. *Geophysical Research Letters*, 38, L14804. <https://doi.org/10.1029/2011GL047968>
- Holton, J. R. (2004). *An introduction to dynamic meteorology* (4th ed.). New York: Elsevier Academic Press.
- Karlsson, B., & Becker, E. (2016). How does interhemispheric coupling contribute to cool down the summer polar mesosphere? *Journal of Climate*, 29(24), 8807–8821. <https://doi.org/10.1175/JCLI-D-16-0231.1>
- Karlsson, B., Körnich, H., & Gumbel, J. (2007). Evidence for interhemispheric stratosphere-mesosphere coupling derived from noctilucent cloud properties. *Geophysical Research Letters*, 34, L16806. <https://doi.org/10.1029/2007GL030282>
- Karlsson, B., McLandress, C., & Shepherd, T. G. (2009). Inter-hemispheric mesospheric coupling in a comprehensive middle atmosphere model. *Journal of Atmospheric and Solar - Terrestrial Physics*, 71(3–4), 518–530. <https://doi.org/10.1016/j.jastp.2008.08.006>
- Karlsson, B., Randall, C. E., Benze, S., Mills, M., Harvey, V. L., Bailey, S. M., & Russell, J. M. III (2009). Intra-seasonal variability of polar mesospheric clouds due to inter-hemispheric coupling. *Geophysical Research Letters*, 36, L20802. <https://doi.org/10.1029/2009GL040348>
- Kleist, D. T., Parrish, D. F., Derber, J. C., Treadon, R., Wu, W.-S., & Lord, S. (2009). Introduction of the GSI into the NCEP Global Data Assimilation System. *Weather and Forecasting*, 24(6), 1691–1705. <https://doi.org/10.1175/2009WAF2222201.1>
- Körnich, H., & Becker, E. (2010). A simple model for the interhemispheric coupling of the middle atmosphere circulation. *Advances in Space Research*, 45(5), 661–668. <https://doi.org/10.1016/j.asr.2009.11.001>
- Lieberman, R. S. (1999). Eliassen-Palm fluxes of the 2-day wave. *Journal of the Atmospheric Sciences*, 56(16), 2846–2861. [https://doi.org/10.1175/1520-0469\(1999\)056%3C2846:EPFOTD%3E2.0.CO;2](https://doi.org/10.1175/1520-0469(1999)056%3C2846:EPFOTD%3E2.0.CO;2)
- Lieberman, R. S. (2002). Corrigendum. *Journal of the Atmospheric Sciences*, 59(17), 2625–2627. [https://doi.org/10.1175/1520-0469\(2002\)059%3C2625:C%3E2.0.CO;2](https://doi.org/10.1175/1520-0469(2002)059%3C2625:C%3E2.0.CO;2)
- Lieberman, R. S., Ortland, D. A., Riggan, D. M., Wu, Q., & Jacobi, C. (2010). Momentum budget of the migrating diurnal tide in the mesosphere and lower thermosphere. *Journal of Geophysical Research*, 115, D20105. <https://doi.org/10.1029/2009JD013684>
- Livesey, N. J., Read, W. G., Wagner, P. A., Froidevaux, L., Lambert, A., Lambert, G. L., et al. (2017). *Earth Observing System (EOS) Microwave Limb Sounder (MLS) Version 4.2x Level 2 data quality and description document, Rep. JPL D-33509 Rev. C*. Pasadena, CA: Jet Propulsion Laboratory.
- Lübken, F.-J. (1999). Thermal structure of the Arctic summer mesosphere. *Journal of Geophysical Research*, 104(D22), 27,803–27,810. <https://doi.org/10.1029/1999JD900076>
- Lumpe, J. D., Bailey, S. M., Carstens, J. N., Randall, C. E., Rusch, D. W., Thomas, G. E., et al. (2013). Retrieval of polar mesospheric cloud properties from CIPS: Algorithm description, error analysis and cloud detection sensitivity. *Journal of Atmospheric and Solar - Terrestrial Physics*, 104, 167–196. <https://doi.org/10.1016/j.jastp.2013.06.007>
- McClintock, W. E., Rusch, D. W., Thomas, G. E., Merkel, A. W., Lankton, M. R., Drake, V. A., et al. (2009). The cloud imaging and particle size experiment on the Aeronomy of Ice in the Mesosphere mission: Instrument concept, design, calibration, and on-orbit performance. *Journal of Atmospheric and Solar - Terrestrial Physics*, 71(3–4), 340–355. <https://doi.org/10.1016/j.jastp.2008.10.011>
- McCormack, J. P., Coy, L., & Hoppel, K. W. (2009). Evolution of the quasi 2-day wave during January 2006. *Journal of Geophysical Research*, 114, D20115. <https://doi.org/10.1029/2009JD012239>
- McCormack, J. P., Coy, L., & Singer, W. (2014). Intraseasonal and interannual variability of the quasi 2-day wave in Northern Hemisphere summer mesosphere. *Journal of Geophysical Research*, 119, 2928–2946. <https://doi.org/10.1002/2013JD020199>
- McCormack, J. P., Eckermann, S. D., Hoppel, K. W., & Vincent, R. A. (2010). Amplification of the quasi-two day wave through nonlinear interaction with the migrating diurnal tide. *Geophysical Research Letters*, 37, L16810. <https://doi.org/10.1029/2010GL043906>
- Merkel, A. W., Thomas, G. E., Palo, S. E., & Bailey, S. M. (2003). Observations of the 5-day planetary wave in PMC measurements from the Student Nitric Oxide Explorer Satellite. *Geophysical Research Letters*, 30(4), 1196. <https://doi.org/10.1029/2002GL016524>
- Molod, A., Takacs, L., Suarez, M., & Bacmeister, J. (2015). Development of the GEOS-5 atmospheric general circulation model: Evolution from MERRA to MERRA2. *Geoscientific Model Development*, 8(5), 1339–1356. <https://doi.org/10.5194/gmd-8-1339-2015>
- Nielsen, K., Siskind, D. E., Eckermann, S. D., Hoppel, K. W., Coy, L., McCormack, J. P., et al. (2010). Seasonal variation of the quasi 5 day planetary wave: Causes and consequences for polar mesospheric cloud variability in 2007. *Journal of Geophysical Research*, 115, D18111. <https://doi.org/10.1029/2009JD012676>
- Pancheva, D., Mukhtarov, P., & Siskind, D. E. (2017). Climatology of the quasi-2-day waves observed in the MLS/Aura measurements (2005–2014). *Journal of Atmospheric and Solar - Terrestrial Physics*, 171, 210–224. <https://doi.org/10.1016/j.jastp.2017.05.002>
- Pendlebury, D. (2012). A simulation of the quasi-two-day wave and its effect on variability of summertime mesopause temperatures. *Journal of Atmospheric and Solar - Terrestrial Physics*, 80, 138–151. <https://doi.org/10.1016/j.jastp.2012.01.006>
- Plumb, R. A. (1982). Zonally-symmetric Hough modes and meridional circulations in the middle atmosphere. *Journal of the Atmospheric Sciences*, 39, 983–991. [https://doi.org/10.1175/1520-0469\(1982\)039%3C0983:ZSHMAM%3E2.0.CO;3B2](https://doi.org/10.1175/1520-0469(1982)039%3C0983:ZSHMAM%3E2.0.CO;3B2)
- Randel, W., Udelhofen, P., Fleming, E., Geller, M., Gelman, M., Hamilton, K., et al. (2004). The SPARC intercomparison of middle-atmosphere climatologies. *Journal of Climate*, 17, 986–1003. [https://doi.org/10.1175/1520-0442\(2004\)17%3C0986:TSIOMC%3E2.0.CO;2](https://doi.org/10.1175/1520-0442(2004)17%3C0986:TSIOMC%3E2.0.CO;2)

- Rienecker, M. M., Suarez, M. J., Todling, R., Bacmeister, J., Takacs, L., Liu, H.-C., et al. (2008). The GEOS-5 Data Assimilation System - Documentation of Versions 5.0.1, 5.1.0, and 5.2.0. In *Technical Report Series on Global Modeling and Data Assimilation 104606* (Vol. 27).
- Salby, M. L. (1981). The 2-day wave in the middle atmosphere: Observations and theory. *Journal of Geophysical Research*, 86(C10), 9654–9660. <https://doi.org/10.1029/JC086iC10p09654>
- Salby, M. L., & Callaghan, P. F. (2001). Seasonal amplification of the 2-day wave: Relationship between normal mode and instability. *Journal of the Atmospheric Sciences*, 58(14), 1858–1869. [https://doi.org/10.1175/1520-0469\(2001\)058%3C1858:SAOTDW%3E2.0.CO;2](https://doi.org/10.1175/1520-0469(2001)058%3C1858:SAOTDW%3E2.0.CO;2)
- Siskind, D. E., & McCormack, J. P. (2014). Summer mesospheric warmings and the quasi 2 day wave. *Geophysical Research Letters*, 41, 717–722. <https://doi.org/10.1002/2013GL058875>
- Siskind, D. E., Stevens, M. H., Hervig, M. E., Sassi, F., Hoppel, K. W., Englert, C. R., & Kochenash, A. J. (2011). Consequences of recent Southern Hemisphere winter variability on polar mesospheric clouds. *Journal of Atmospheric and Solar - Terrestrial Physics*, 73(13), 2013–2021. <https://doi.org/10.1016/j.jastp.2011.06.014>
- Stevens, M. H., Lieberman, R. S., Siskind, D. E., McCormack, J. P., Hervig, M. E., & Englert, C. R. (2017). Periodicities of polar mesospheric clouds inferred from a meteorological analysis and forecast system. *Journal of Geophysical Research: Atmospheres*, 122, 4508–4527. <https://doi.org/10.1002/2016JD025349>
- Torrence, C., & Compo, G. P. (1998). A practical guide to wavelet analysis. *Bulletin of the American Meteorological Society*, 79(1), 61–78. [https://doi.org/10.1175/1520-0477\(1998\)079%3C0061:APGTWA%3E2.0.CO;2](https://doi.org/10.1175/1520-0477(1998)079%3C0061:APGTWA%3E2.0.CO;2)
- von Savigny, C., Robert, C., Bovensmann, H., Burrows, J. P., & Schwartz, M. (2007). Satellite observations of the quasi 5-day wave in noctilucent clouds and mesopause temperatures. *Geophysical Research Letters*, 34, L24808. <https://doi.org/10.1029/2007GL030987>
- Wu, W.-S., Purser, R. J., & Parrish, D. F. (2002). Three-dimensional variational analysis with spatially inhomogeneous covariances. *Monthly Weather Review*, 130(12), 2905–2916. [https://doi.org/10.1175/1520-0493\(2002\)130%3C2905:TDAVWS%3E2.0.CO;2](https://doi.org/10.1175/1520-0493(2002)130%3C2905:TDAVWS%3E2.0.CO;2)